CHAPTER 4

VALIDATION OF THE PARALLEL MODEL

Summary

The power conversion efficiency of solar cells based on a conjugated polymer (donor) and a fullerene derivative (acceptor) is very sensitive to the morphology of the active layer. One detrimental feature, which is often encountered in non-optimal morphologies, is the occurrence of fullerene blobs in a finely-mixed matrix containing both donor and acceptor material. In this chapter, the effects of such fullerene blobs are studied in detail with a three-dimensional drift-diffusion model. The influence of blob size and shape, and matrix composition are quantified. The total current flowing out of the solar cell can be split up in a part which comes from the interfacial region between the acceptor phase and the mixed phase, and a part that stems from the mixed phase itself. Depending on the bias voltage and the morphology, one or the other contribution is dominant. It is shown how both contributions can be computed with a simple one-dimensional drift-diffusion simulator.

4.1 Introduction

It is widely known that the morphology of the active layer is one of the main factors that determine the efficiency of BHJs.[1–3] The length scale of the separation between the donor and the acceptor material is relevant to the processes of generation and transport of free charges.[4–6] Also the composition[6–8] and the crystallinity[9,10] of the donor and acceptor domains, and the existence of percolation pathways to extract the photogenerated charges[11,12] play an important role.

Many studies have addressed the possibilities of controlling the morphology by means of the processing conditions. For solution-based processing such as spin-coating, doctor blading, slot dye coating or inkjet printing it has been shown that the goal of optimizing the morphology has to be pursued since the preparation of the solution, by choosing the proper solvent,[13–15] co-solvents,[16,17] and additives.[18] The deposition process[19,20] and the post-deposition treatments, *e.g.* thermal[21] or solvent[22] annealing, define the final morphology of the active layer.

It would be greatly beneficial for the optimization of BHJs to develop accurate models to predict the morphology based on properties of the materials and processing conditions. Furthermore, a model to accurately relate the morphology of the active layer and the efficiency of the device[23–27] is essential to orient the optimization process towards the best-performing morphology.

Depending on the processing conditions, the deposition of polymer:fullerene blends can result in an homogeneous, finely dispersed mixture of polymer and fullerene, or in a phase separated system with large (hundreds of nm), rather pure domains of fullerene embedded into a polymer-rich matrix, similar to the morphology depicted in Figure 4.1. This has been observed for many polymer:fullerene systems;[6,13,28–31] it is therefore interesting to understand how the phase separation in these blends affects the performance.

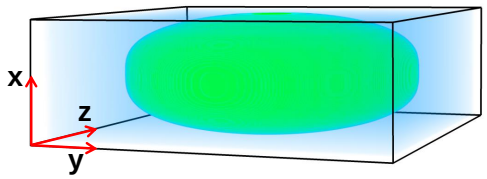

Figure 4.1: Schematic representation of a typical fullerene blob embedded in a polymer-rich matrix. The electrodes are parallel to the $y-z$ plane.

In the previous chapters we analysed PDPP5T:[70]PCBM blends, showing how it is possible to use a one-dimensional (1D) drift-diffusion model[32] to simulate the JV characteristics of such PDPP5T:[70]PCBM blends, either homogeneous or phase separated. For the latter case, we treated the total current as the sum of two parallel contributions,

coming from different areas of the active layer. From now on in this chapter, this approach will be referred to as "parallel model".

Here we present a three-dimensional (3D) drift-diffusion model and use it to study the influence of large compositional inhomogeneities on efficiency. This model includes the solution of the exciton diffusion equation in three dimensions; the effects of space charge, generation and recombination of free charge carriers, and injection and extraction at the electrodes. We present the results of our simulations for a large number of morphologies, showing the effect of morphological features on the efficiency of the device. In particular, we discuss the impact of varying the size of the acceptor domains and the composition of the donor-rich matrix surrounding them. Additionally, the influence of the presence of a thin, donor-rich skin layer at the top and at the bottom of the acceptor domains is investigated. The simulations are done by varying only one parameter for each one; in this way, we are able to disentangle the effects of the different morphological features.

According to the 3D results, the device performance is mostly affected by the composition of the mixed phase; this is in agreement with the simulation performed with the parallel model, which highlights that the dominant component of the total current comes from this phase. This conclusion is not a general rule; the relative importance of the mixed phase depends on the morphology, and we also show situations in which the total current is dominated by the charges flowing at the interfacial region between acceptor and mixed phase.

The 3D simulation of the JV curves of BHJs requires a longer time if compared with the 1D parallel model; in return, it enables simulation of systems presenting coarse phase separation and it gives a detailed picture of the physical processes occurring in the active layer. The agreement of the 3D model and the parallel model indicates that the latter can be also used to describe a certain number of systems with phase-separated morphology.

4.2 Modelling approach

In this section we discuss the choice of the material parameters that we use in the simulations. We then briefly introduce the two models that we compare in this chapter: the 3D drift-diffusion model and the parallel model.

4.2.1 Materials parameters

Drift-diffusion modelling of the JV characteristics of organic solar cells, either 3D and 1D, is performed by using one set of materials parameters. The energy difference between the lowest unoccupied molecular orbital of the acceptor material (LUMO_A) and the highest occupied molecular orbital of the donor material (HOMO_D) is set to 1.1 eV; for the relative dielectric constant ε_r, a typical value of 3 is used. The exciton diffusion length inside the pure acceptor domains is assumed to be 20 nm. We note that light absorption by fullerene derivatives and subsequent hole transport to a donor polymer

can significantly contribute to the current generation in organic solar cells.[33] In general, most of the incident light is absorbed by the donor polymer. Nevertheless, our simulations assume the two materials to absorb the same fraction of the incident light; in this way, when the overall composition of the blend changes the overall absorption is not modified, and we can study the effect of morphological features excluding modification to the JV curves due to different excitons generation rates.

The charge transport parameters are based on the experimental data presented in Chapter 2 for PDPP5T:[70]PCBM blends. The transport of electrons and holes in these blends is dominated by the electric-field dependency of the mobility; Figure 2.6 presents the mobilities of electrons and holes as a function of the volume fraction of acceptor (φ) in the blend. The electron mobility strongly depends on the acceptor concentration, the electrons being transported by the acceptor molecules; hole transport occurs through the donor and its efficiency its rather unaffected by the presence of the acceptor at these donor/acceptor ratios. Our model considers the bimolecular recombination to be the only recombination mechanism of free charges active in the device. The bimolecular recombination of free charges in materials with low mobility is often described with the Langevin recombination rate[34], although a reduction of the bimolecular recombination strength given by Langevin has been often observed in polymer:fullerene systems.[35,36] This deviation can be included into the drift-diffusion model by using a prefactor $\gamma_{\text{pre}} < 1$ for the recombination rate. We keep the prefactor equal to unity for the 3D simulation; a reduction of the bimolecular recombination strength is needed to correctly simulate the interfacial component of the current with the parallel model (see Section 4.3.2).

The parameters presented above may be different for specific donor/acceptor combinations; however, our conclusions do not depend on this particular choice of values.

4.2.2 Three-dimensional numerical model

The morphologies that we consider feature a mixed phase consisting of intimately mixed donor and acceptor material and a pure acceptor phase. Light is absorbed in both phases. Excitons in the mixed phases are assumed to yield free charge carriers with unity quantum efficiency. The excitons in the pure acceptor phase undergo diffusion and may either decay or be quenched at an interface with the mixed phase (yielding free charge carriers) or with the electrodes. Exciton quenching at the electrodes does not yield free carriers and is a loss process. To calculate how many excitons yield free carriers at the interface between the acceptor and the mixed, we solve the exciton diffusion equation[25]

$$0 = -\frac{X(\vec{r})}{\tau} + D_x \nabla^2 X(\vec{r}) + g, \tag{4.1}$$

where X is the exciton density, τ is the exciton lifetime, D_x is the exciton diffusion constant, and g is the volume generation rate of excitons. For simplicity, g is taken uniform across the layer. At all quenching interfaces we require X be zero. Free charge carriers

are generated at a rate equal to

$$G_A = G_D = D_x \frac{X}{(\delta x)^2}, \tag{4.2}$$

where δx is the grid spacing. The current continuity equations read [25]

$$\mathrm{div}\vec{J}_n = q\,(G - R) \tag{4.3a}$$

$$\mathrm{div}\vec{J}_p = -q\,(G - R)\,, \tag{4.3b}$$

where $\vec{J}_{n(p)}$ is the electron (hole) current density. The bimolecular recombination rate R is given by

$$R = \gamma n p, \tag{4.4}$$

where γ is the Langevin recombination rate constant given by

$$\gamma = \frac{q}{\varepsilon}\left(\mu_n + \mu_p\right). \tag{4.5}$$

The flow of charge carriers is governed by the drift-diffusion equations. [37] In the mixed phase, both electrons and holes are present and we have for electrons

$$J_p = -qn\mu_n \nabla V + qD_n \nabla n \tag{4.6}$$

and for holes

$$J_p = -qp\mu_p \nabla V - qD_p \nabla p \tag{4.7}$$

We assume that the Einstein relation between mobility and diffusivity $D_{n,p}$ holds. [? ?] The electron and hole mobility are functions of the local donor/acceptor ratio according to Figure 2.6. In the pure acceptor phase, only electrons are considered. The electrostatic potential is solved from the Poisson equation;

$$\nabla^2 V = \frac{q}{\varepsilon}\left(n - p\right). \tag{4.8}$$

The boundary condition on the potential is given by

$$q\left(V_L - V_0 + V_a\right) = W_{\text{anode}} - W_{\text{cathode}}, \tag{4.9}$$

where V_L and V_0 are the potentials at either electrode, V_a is the applied voltage, and W_{anode} and W_{cathode} are the anode and cathode work function, respectively.

The boundary condition on the electron (hole) density at the electrodes is given by [25]

$$n(p) = N_{cv} \exp\left(-\frac{\phi_{A(D)}}{V_t}\right), \tag{4.10}$$

where $\phi_{A(D)}$ is the barrier between the LUMO (HOMO) of the acceptor (donor) and the electrode and N_{cv} is the effective density of states. First, Equation 4.1 is solved to yield the exciton density and corresponding generation rate of free charge carriers. Then, an iterative approach is used to solve the system of Equation 4.2−4.10 self-consistently. [37]

4.2.3 1D model and parallel approach

The JV characteristics of organic bulk heterojunctions with homogeneous morphology can be modelled with a 1D drift-diffusion approach. We use a model that describes the active layer as one effective medium, by considering the LUMO of the acceptor material and the HOMO of the donor as the valence and conduction band of an effective semiconductor sandwiched between two electrodes. The model takes into account generation, recombination and transport of charge carriers, as well as the effect of space charge on the electric field. A detailed description of the model is given in Ref. 32.

This 1D approach can be used to consistently describe the JV curves of homogeneous blend, in which the segregation length is much smaller than the device thickness. In this chapter we show how it is possible to apply it also to model bulk heterojunctions characterized by a coarse phase separation. For active layers with morphology similar to the one shown in Figure 4.1, with large, almost circular and rather pure acceptor domains dispersed into a donor-rich phase, it is reported in Chapter 3 that the total current can be described as the sum of two separate contributions:

$$J_{\text{tot}} = J_{\text{mixed}} + J_{\text{interface}} \tag{4.11}$$

where J_{mixed} is the contribution from the mixed phase far from the acceptor domains and $J_{\text{interface}}$ is the contribution from the region surrounding the blob/matrix interface. The areas from which the two contributions come are depicted in Figure 3.1b. For a description of the local contribution to the total photocurrent, see Section 3.2.3.

If skin layers of donor-rich phase are present at the electrodes, their contribution has to be taken into account. The skin layer at the anode, below the acceptor blobs, is included in the calculation of $J_{\text{interface}}$, together with the lateral region of width W_O. The holes generated in this skin layer can reach the anode, while the electrons moves vertically to the blob and are transported to the cathode. As we show below, the situation is different in a skin layer at the cathode: here, most of the holes would have to travel laterally along the blob surface for a long distance (typical blob diameters are in the order of magnitude of hundreds of nm) to be then transported to the anode through the mixed phase; since such a long lateral movement is unlikely to take place, we assume that the charges generated in the skin layer at the cathode does not contribute to $J_{\text{interface}}$.

In the previous chapter the parallel model was used to simulate the experimental JV curves measured for PDPP5T:[70]PCBM solar cells with coarse phase separation. Here we employ it to fit the data generated by the 3D simulation. We use the same parameters that we employ as input for the 3D code: thickness of the sample and of the skin layers, size of the acceptor domains, acceptor concentration in the mixed phase are therefore fixed, leaving W_O as the only fit parameter. It has to be noted that in the previous chapter the model had one parameter W_I, which represented the width of the region inside the blobs that contributes to J_{mixed}. W_I is not needed in this chapter: the excitons generated inside the blobs and contributing to the generation of free charges are taken into account by solving 3D exciton diffusion equation. Furthermore, due to the compu-

tational limits of the 3D model, the thickness of the mixed phase has to be equal to the thickness of the acceptor phase ($T_M = T_A = L$).

4.3 Outcome of the simulations

In this section the results of the simulations performed with the 3D model and with the parallel approach are presented and discussed.

4.3.1 3D calculations

We analyse the influence of phase segregation, skin layers, matrix composition and size of the pure domains on the performance of the device. The morphological features of the devices simulated in this chapter are listed in Table 4.1. It should be noted that all the simulations have been done considering the case of pure acceptor domains embedded into a donor-rich mixed phase. The outcomes would be similar in the situation of pure donor phase in acceptor-rich matrix, which for reason of brevity we do not discuss here.

Table 4.1: Parameters for the simulation of the JV curves of the devices presented in this chapter.

Simulation	Figure	L [nm]	D [nm]	S_a [nm]	S_c [nm]	φ_{mixed}	V_a
1	4.2	140	0	0	0	0.25	0
2	4.2, 4.4-4.9	140	300	0	0	0.25	0.40
3	4.2	140	0	0	0	0.55	0
4	4.3	140	300[a]	4	4	0.25	0.27
5	4.3	140	300[a]	4	4	0.25	0.30
6	4.3	140	300[a]	4	4	0.25	0.32
7	4.3, 4.4	140	300	4	4	0.25	0.38
8	4.4	140	300	4	0	0.25	0.39
9	4.4	140	300	0	4	0.25	0.39
10	4.5	140	300	0	0	0.25[b]	0.40
11	4.5	140	300	0	0	0.25[c]	0.40
12	4.6	140	300	0	0	0.20	0.40
13	4.6	140	300	0	0	0.30	0.40
14	4.7	140	240	0	0	0.25	0.26
15	4.7, 4.9	140	180	0	0	0.25	0.14
16	4.8	70	300	0	0	0.25	0.40
17	4.8	280	300	0	0	0.25	0.40
18	4.9	140	180	0	0	0.25	0.44

a) Not cylindrical blobs: the maximum diameter is indicated.
b) Depletion: 10 nm with $\varphi_{\text{mixed}} = 0.20$ around the blobs.
c) Enrichment: 10 nm with $\varphi_{\text{mixed}} = 0.30$ around the blobs.

Phase segregation

Figure 4.2 presents the simulated JV characteristics of three solar cells which differ in acceptor concentration and in morphology. Two of them have the same acceptor content (55 vol.%) and are characterized by different amount of phase separation. The third one has a lower amount of acceptor (25 vol.%) and an homogeneous morphology. The latter device is the one with the lowest efficiency: its performance is strongly limited by the low electron mobility that characterizes the blend with such a low acceptor concentration (see Figure 2.6). Furthermore, the electric field dependency of the electron mobility reduces the fill factor of the solar cell to a value around 33%, lower than the theoretical value of 42% predicted by Mihailetchi et al.[38] for space-charge limited photocurrent (see Section 3.4.1).

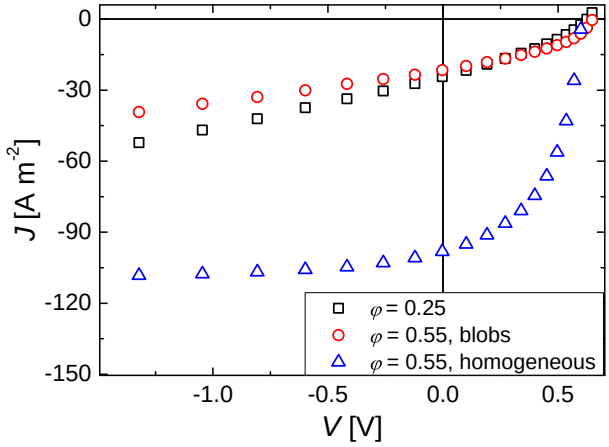

Figure 4.2: Simulated JV curves for different overall acceptor concentration φ and for different extent of phase segregation. The device with coarse phase separation has cylindrical blobs with $D = 300$ nm embedded in a mixed phase with $\varphi_{\text{mixed}} = 0.25$. In this plot are displayed Simulation 1 (black squares), 2 (red circles) and 3 (blue triangles).

The addition of more acceptor to a homogeneous blend greatly enhances the efficiency; the device with 55 vol.% of acceptor and homogeneous morphology presents a six-fold enhancement of the PCE if compared with the device with 25 vol.% acceptor. The reasons for this considerable improvement are the increase of electron mobility and the reduction of its field dependency upon increasing the acceptor volume fraction (Figure 2.6). However, the beneficial effect of having more acceptor in the blend is lost if the acceptor molecules aggregate in large domains. The curve shown in Figure 4.2 for coarse phase segregation represents the JV of a device with cylindrical acceptor domains with diameter $D = 300$ nm. In this case, not all the photogenerated excitons are quenched: the excitons generated at a large distance from the acceptor/donor interface

cannot reach it to be dissociated and are lost. By solving the exciton diffusion equation in 3D, we obtain a 65% exciton quenching efficiency; this partly explains the reduction of short circuit current with respect to the homogeneous blend with the same acceptor content. The low content of acceptor in the matrix (φ_{mixed}) surrounding the blobs further reduces the current and the fill factor due to space charge effect and electric field dependency, as discussed above.

Blob shape

The JV curve shown in Figure 4.2 for the case of phase separation has been calculated for cylindrical blobs. In real devices the acceptor aggregates do not have such a perfect shape; in general their lateral surface is curved, a typical blob shape is the one displayed in Figure 4.1. We investigate the effect of the shape of the blobs by means of the 3D model. We draw the acceptor domains volume using the equation

$$\left(\frac{2x}{L}\right)^m + \left(\frac{y}{R}\right)^2 + \left(\frac{z}{R}\right)^2 \leq 1, \tag{4.12}$$

where L is the sample thickness, R is the radius of the blobs at their largest horizontal cross-section, and x, y and z are the vertical and the horizontal coordinates, respectively. The shape of the volume depends on the value of the exponent m. An ellipsoid is obtained for $m = 2$; we also run the simulation for $m = 3$ and $m = 4$, and we compare the results with the simulation of the case of cylindrical blobs. 4 nm of donor-rich skin layers (with the same composition of the mixed phase) are added at the two contacts, for every morphology. From the results plotted in Figure 4.3 it appears that the shape of the blobs does not play a significant role; only a slight reduction of the photocurrent is observed going from the ellipsoid blobs to the cylinders, due to a reduction of the exciton quenching efficiency. Moreover, if the blob has a curved lateral surface, the effect of the skin layer at the cathode is slightly modified (see next Section). To disentangle the effect of the shape from the effect of blob size and distribution, we simulate from now on only cylindrical blobs. This also greatly simplifies the calculations both for the 3D and for the parallel model.

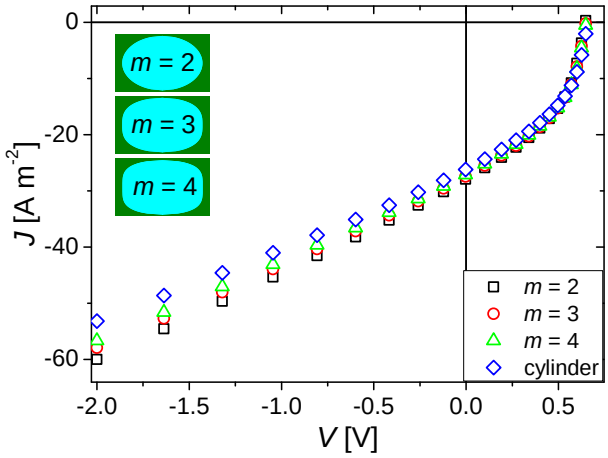

Figure 4.3: Simulated JV curves for different shapes of the acceptor domains. The shapes have been drawn using Equation 4.12 for $m = 2$, 3 and 4 and are shown in the inset. Cylindrical blobs have also been simulated. In this plot are displayed Simulation 4 (black squares), 5 (red circles), 6 (green triangles) and 7 (blue diamonds).

Skin layers

It has been observed experimentally that thin skin layers of mixed phase are often present at the top and at the bottom of the pure domains.[15,39] We analyse the influence of this layers on the overall device efficiency. Using a 3D model it is possible to include a thin layer of mixed phase at each of the two contacts. The simulations shown in Figure 4.4 present the effect of 4-nm thick skin layers at the anode, at the cathode or at both contacts. The acceptor concentration in the skin layer is the same as in the rest of the matrix (25 vol.%). The skin layer at the anode is beneficial for the device performance: its presence enhances the photogenerated current, because it increases the donor:acceptor interface and more excitons can be dissociated. This yields free charges in the skin layer at the anode: the holes are easily collected by the close-by electrode, and the electrons move vertically to the blob and are subsequently transported to the cathode. The presence of a skin layer at the cathode does not give the same effect. Also in this case more excitons are quenched due to a larger donor/acceptor interface. But the holes generated in this thin layer cannot travel through the pure acceptor blob to reach the anode; they should instead move laterally along the surface of the blob and then vertically through the mixed phase. However, the lateral dimension of the blobs is so large that holes undergo bimolecular recombination before reaching the edge of the blobs, and are lost. Therefore, the skin layer at the cathode does not contribute to the photocurrent. In case

of non-cylindrical blobs (Figure 4.3), some of the holes generated in the skin layer at the cathode are able to reach the anode and the current is slightly enhanced.

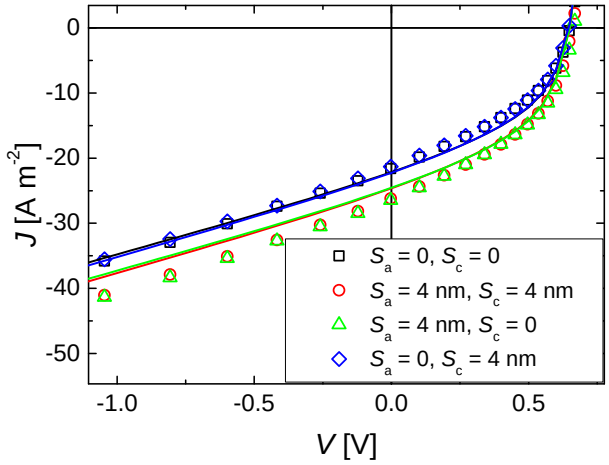

Figure 4.4: Simulated JV curves for devices with and without skin layers at the two electrodes. The symbols represent the 3D simulations, the solid lines are calculated with the parallel model. In this plot are displayed Simulation 2 (black squares), 7 (red circles), 8 (green triangles) and 9 (blue diamonds).

Interestingly, our results do not show any detrimental effect of the skin layer at the cathode. One may argue that a donor-rich layer at the cathode might hinder the extraction of electrons; it has been shown instead by Lyons *et al.*[40] that the photocurrent is minimally affected as long as the electron transporting material is present in the skin layer above a certain concentration threshold (15 vol.%). Our results, obtained for skin layer with 25 vol.% acceptor concentration, are fully in agreement their predictions.

Having outlined the effect of the skin layers on the photogenerated current, we can exclude them for the other simulations and focus on the importance of the composition of the mixed phase and on the dimension and the number density of the pure acceptor domains.

Depletion/enrichment close to the blobs

Up to now, we have shown the results obtained for systems presenting a homogeneous matrix. When pure domains of acceptor are formed, it is possible that the acceptor concentration in the surrounding matrix will not be constant: there may be either an increase in acceptor concentration moving towards the pure phase, or a depletion region in which the acceptor concentration is lower than in the rest of the matrix. We simulate these two cases by adding a thin region (10 nm) around the blobs with a concentration of acceptor

slightly higher (30 vol.%) or slightly lower (20 vol.%) than in the mixed phase far from the blobs (25 vol.%). The results of these simulations are in Figure 4.5. The short circuit current increases to a certain extent by adding more acceptor around the blobs. This is due to the fact that an higher concentration of acceptor facilitates the lateral movement of electrons from the mixed phase towards the acceptor phase, through which they are efficiently transported to the cathode.

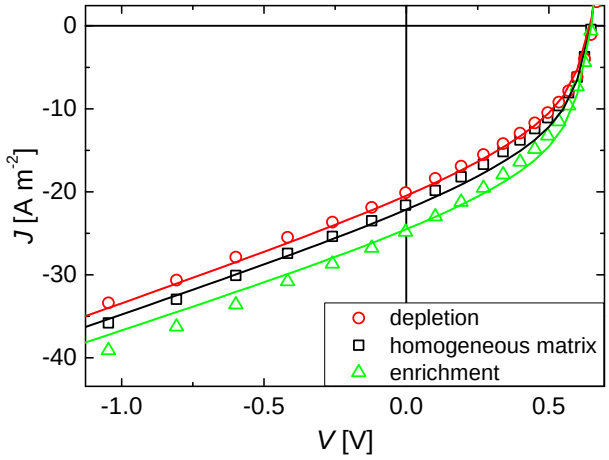

Figure 4.5: Simulated JV curves for devices with different acceptor concentration in the mixed phase in the proximity of the blobs. The symbols represent the 3D simulations, the solid lines are calculated with the parallel model. The homogeneous matrix has $\varphi_{\text{mixed}} = 0.25$; 10 nm with $\varphi_{\text{mixed}} = 0.20$ and $\varphi_{\text{mixed}} = 0.30$ are added around the blobs in the case of depletion and enrichment, respectively. In this plot are displayed Simulation 2 (black squares), 10 (red circles), and 11 (green triangles).

Matrix composition

We verify the impact of the overall active layer composition by keeping the size of the acceptor domains constant (D = 300 nm) and modifying the acceptor concentration in the mixed phase. Figure 4.6 shows the simulated JV curves for three different compositions of the mixed phase. It is evident how important is the effect of the acceptor concentration in the matrix on the device performance: increasing it from 20 vol.% to 30 vol.% results in more than a factor of 2 enhancement of the short circuit current. This improvement is partly explained by the more efficient lateral transport of electrons towards the blobs through the matrix with more acceptor. But, as shown in the previous sub-section, this gives only a modest increase of the photocurrent. The main cause of the increased performance is the large enhancement of the electron mobility when the acceptor concentration in the matrix is increased from 20 vol.% to 30 vol.% (Figure 2.6),

which reduces the effect of space charge in the current flowing vertically through the mixed phase.

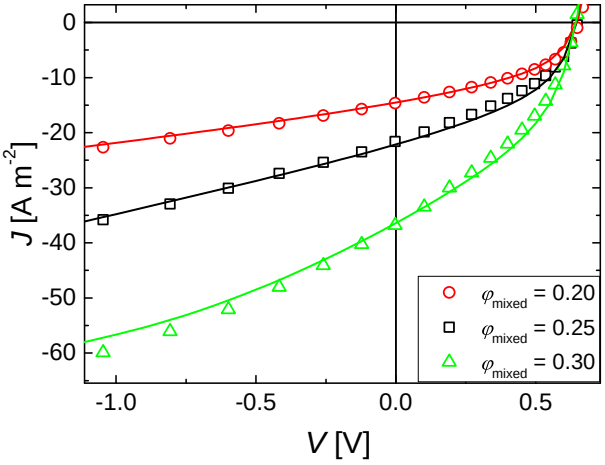

Figure 4.6: Simulated JV curves for devices with different acceptor concentration in the mixed phase. The symbols represent the 3D simulations, the solid lines are calculated with the parallel model. In this plot are displayed Simulation 2 (black squares), 12 (red circles), and 13 (green triangles).

Blob size

We simulate devices with constant matrix composition (25 vol.% acceptor) and different blob diameters, from 180 to 300 nm. The corresponding JV curves are reported in Figure 4.7. The impact of the blob size on the efficiency is relatively low: only a slight reduction of the short-circuit current density (J_{sc}) and increase in fill-factor (FF) are observed upon increasing the diameter of the blobs. The reduction in the current is assigned to a less efficient exciton quenching in the pure phases; the FF enhancement is due to the fact that a larger fraction of the current is transported through the interfacial region (see next Section).

Remarkably, both Figures 4.6 and 4.7 represent the effect of the overall composition of the active layer. In Figure 4.6 it is shown how an increase of the overall acceptor volume fraction from 52% to 58% (corresponding to 20 vol.% and 30 vol.% of acceptor in the matrix, respectively) almost doubles the PCE of the cell. For the JV curves presented in Figure 4.7 the increase in acceptor volume fraction is even bigger: from 35.8% in case of D = 180 nm to 55% in case of D = 300 nm. This does not translate into the same effect on the performance of the cell: the PCE is almost unaffected, and it rather diminishes, though in a modest amount, for higher volume fractions of acceptor. The explanation of this different effect of the overall composition will be clarified in Section 4.3.2.

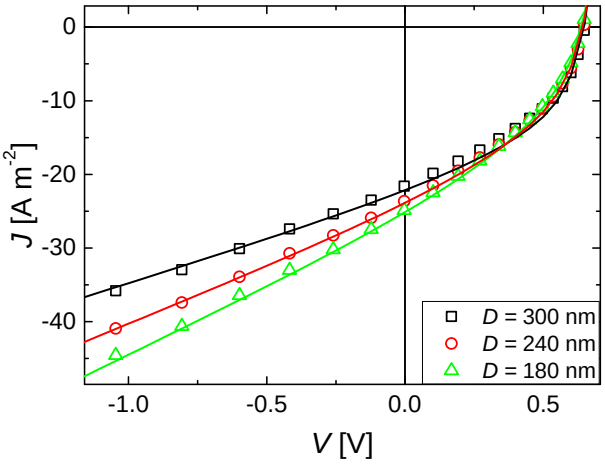

Figure 4.7: Simulated JV curves for devices with different diameters of the pure acceptor domains. The symbols represent the 3D simulations, the solid lines are calculated with the parallel model. In this plot are displayed Simulation 2 (black squares), 14 (red circles), and 15 (green triangles).

Thickness of the active layer

Figure 4.8 presents the JV curves for simulated devices with different thickness of the active layer. The size and shape of the blobs and the composition of the matrix are the same for the three simulations. In the mixed phase of the thickest device negative space charge is built up which strongly limits the current coming from this phase. For the thinnest device, the current in reverse bias is not space charge limited but saturates at its maximum value qGL.

Number of blobs

Lastly, we consider the effect of blob density. Keeping the diameter of the blobs constant (D = 180 nm), we modify the distance between them. By doing so, the volume fractions of acceptor and mixed phase are changed. The simulated JV curves are reported in Figure 4.9. When the blobs are closer to each other, and the volume fraction of acceptor phase is larger, the fraction of current transported in the interfacial region between acceptor and mixed phase is increased and this translates into an enhancement of the fill factor, due to the good electron transport that characterizes the current flowing in this region.

The density of the pure acceptor domains mainly influences the shape of the JV characteristic, and hence the fill factor. A small effect is visible for J_{sc}: the simulated device with higher blob density has a lower exciton quenching efficiency, which gives a lower current. It should be noted that this does not depend on the quenching efficiency of

the pure phase: the blobs have, in both simulations, the same shape and size, and the fraction of excitons generated into the acceptor phase and able to reach the interface is the same. The difference in the overall quenching efficiency is solely due to the different volume fractions of pure acceptor phase.

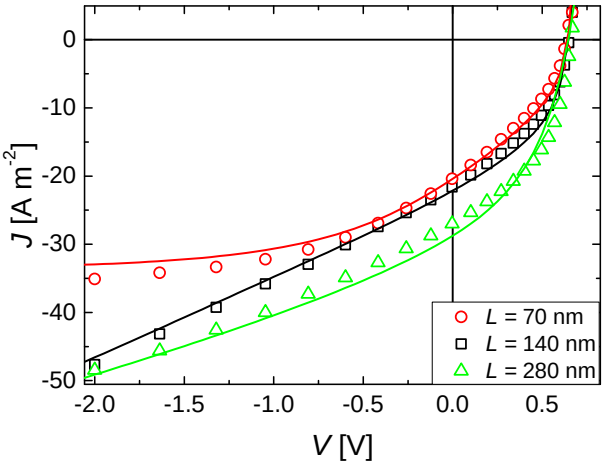

Figure 4.8: Simulated JV curves for devices with different thicknesses. The symbols represent the 3D simulations, the solid lines are calculated with the parallel model. In this plot are displayed Simulation 2 (black squares), 16 (red circles), and 17 (green triangles).

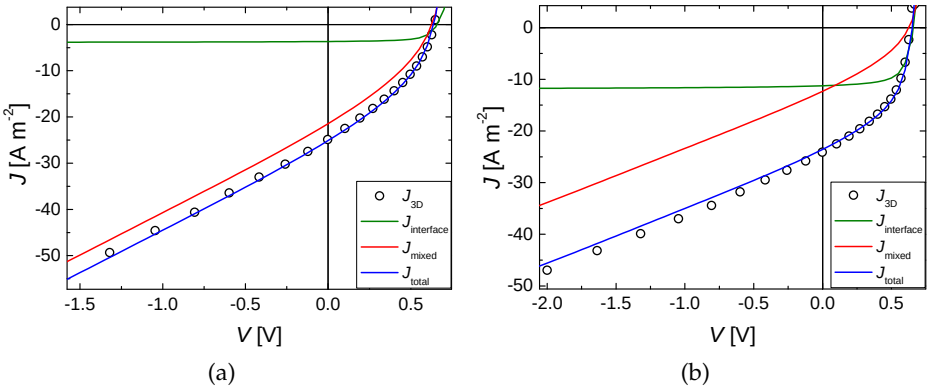

Figure 4.9: Simulated JV curves for devices with different number densities of the acceptor blobs. The volume fraction of the acceptor pure phase is a) 0.14 (Simulation 15) and b) 0.44 (Simulation 18) The symbols represent the 3D simulations, the solid lines are calculated with the parallel model.

4.3.2 Parallel model

We reproduce the JV curves simulated with the 3D model using the parallel approach described in Section 4.2.3. The results are represented as solid lines in Figure 4.4−4.9. The good agreement between the two models for all the simulated cases confirms the possibility to apply the 1D parallel approach to simulate the JV characteristics of devices with coarse phase separation. A further validation of the parallel model is obtained by calculating the two components J_{mixed} and $J_{\text{interface}}$ with the 3D model. We perform this calculation for Simulation 2. $J_{\text{mixed,3D}}$ is calculated as the contribution to the total current of points far away from the acceptor blob. $J_{\text{interface,3D}}$ is taken as the contribution of the all points within the blue region of Figure 3.1b, that is, the outer part of the blob and the region around it (W_O) in which the electrons move laterally towards the blob. The single contributions to the total current calculated with the 3D and with the 1D model for Simulation 2 are compared in Figure 4.10. The 3D results agree very well with those obtained with the parallel model.

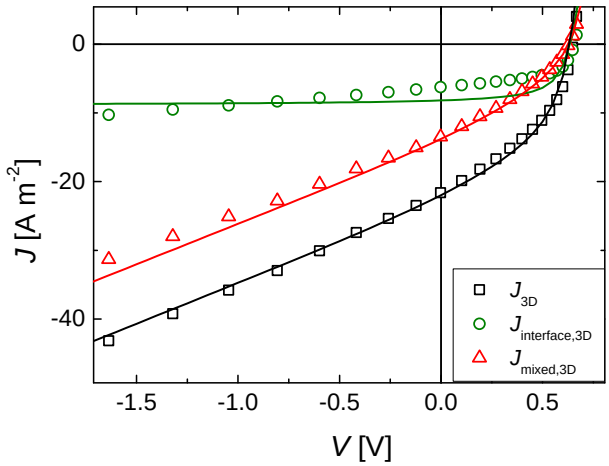

Figure 4.10: Simulated JV curves for the total current and the two separated components calculated with the 3D (symbols) and with the parallel (lines) models. This plot displays Simulation 2.

As written in Section 4.2.1, the strength of the bimolecular recombination is reduced for the simulation of $J_{\text{interface}}$. This reduction is necessary to compare the results of the parallel approach to the ones of the 3D model. This latter method uses Equation 4.4 and 4.5 to calculate the recombination rate. As the recombination occurs in the mixed phase, the values of hole and electron mobilities in this phase are used by the 3D code. But when we simulate $J_{\text{interface}}$ with the 1D approach, we use the significantly higher value of the electron mobility in the blobs. This would lead to an increased rate of bimolecular recombination; in order to correct for this, we reduce the strength of the bimolecular

recombination by applying a prefactor $\gamma_{\text{pre}} \leq 1$ to Equation 4.5. We determine γ_{pre} by fitting the open circuit voltage, since it is known that this parameters is largely affected by the recombination rate.[41] For every simulation performed with the parallel model, the value of the prefactor expressing the reduction of the bimolecular recombination strength for $J_{\text{interface}}$ is $\gamma_{\text{pre}} = 0.1$.

The parallel model has one fit parameter, W_O, which is the width of the region around the blobs in which the electrons move laterally towards them. This parameter partly determines the distribution of the total current between $J_{\text{interface}}$ and J_{mixed}. The values of W_O used for every simulation are reported in Table 4.1. As expected, W_O is larger when the concentration of acceptor in the matrix is increased, because a larger volume fraction of acceptor means higher electron mobility, and thus the lateral movements of electrons towards the blobs is facilitated. It is interesting to observe that the extent of the lateral transport of electrons in the mixed phase does not only depend on the composition of the matrix, but also on the size of the blobs: W_O is reduced for smaller acceptor domains. We have simulated JV curves with even larger blobs than the one reported in Figure 4.7 (data not shown) and fit them with the parallel model. Figure 4.11 represents the fit parameter W_O as a function of the blob diameter. Beyond a certain size of the pure acceptor domains, W_O saturates at a value of 12 nm. We assign the reduction of W_O for small blob diameters to the increased density of electrons in smaller blobs, which reduces their capacity to accept further electrons from the surrounding matrix.

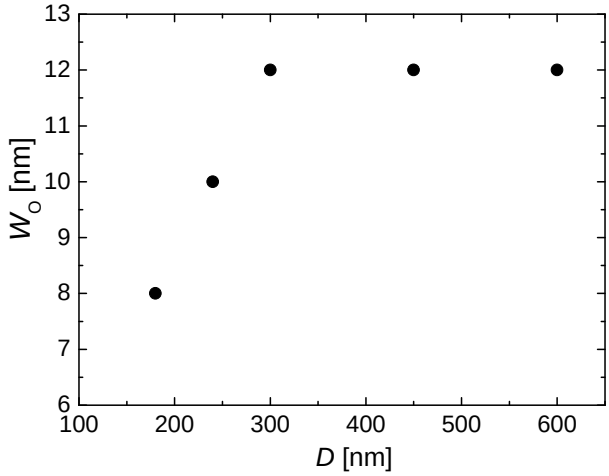

Figure 4.11: The fit parameter W_O as a function of the blob diameter. For all these simulations, the blobs are cylindrical, $\varphi_{\text{mixed}} = 0.25$ and no skin layers are included.

Figure 4.9a and b represent the fits of the 3D simulated points for different blob density. In addition, in these plots are shown the two parallel components, $J_{\text{interface}}$ and J_{mixed}. The parallel approach explains the difference in fill-factor when devices with dif-

ferent blob density are compared: it is evident that increasing the density of the domains enhances the fraction of current transported through the interfacial region, where the electron mobility is high. The fill factor is higher for $J_{\text{interface}}$, which is characterized by a balanced transport of charges. It is therefore predictable an enhancement of FF when $J_{\text{interface}}$ dominates the total current.

Qualitatively, increasing the concentration of acceptor in the mixed phase or decreasing the size of the acceptor blobs have the same effects on the JV characteristics, namely an increase in J_{sc} and a reduction of FF. We observed the same trends in experimental JV curves from PDPP5T:[70]PCBM devices in the previous chapter. However, in the experimental data the size of the blobs and the composition of the matrix have been varied at the same time; in this work instead we disentangle the effects of each of this two morphological features. We are thus able to see how important to the performance of the device each one of them is. Our results indicate that a small variation of the overall of the acceptor concentration in the matrix has a bigger impact than the larger variation produced by the change in blob size. The different roles played by the changing the overall composition of the blend through modification of the matrix composition (Figure 4.6) or the blob size (Figure 4.7) depends on which of the two contributions, $J_{\text{interface}}$ and J_{mixed}, is dominant. The values of $J_{\text{interface}}$ and J_{mixed} at short circuit current for each simulation are listed in Table 4.2, together with the fraction of the total current that they represent ($\%_{\text{interface}}$ and $\%_{\text{mixed}}$, respectively). In most of the cases presented here, J_{mixed} is the dominant component of the total current, and this explains why varying the composition of the mixed phase is more effective than varying the blob size. We suppose that the relative importance of the two features would change in the case of dominant $J_{\text{interface}}$.

Splitting the total current into two components makes it easier to explain the results observed for devices with different thickness, which stem from the different transport properties that characterizes $J_{\text{interface}}$ and J_{mixed}. The latter current is strongly limited by space charge, due to the large difference between the mobilities of electrons and holes. When the film is thin, the space charge effect is reduced and the current saturates at the value qGL; G is given by the total excitons quenching efficiency, calculated by the solution of the 3D excitons diffusion equation. For the 280 nm thick devices (see Figure 4.8), J_{mixed} is so limited by the build-up of space charge that most of the current comes from the interfacial region. At intermediate thickness, both the currents contribute to J_{total} and the effect of space charge in the matrix becomes evident in reverse bias, where J_{mixed} dominates.

Table 4.2: Parallel model results: values of the parameter W_0 used to fit the 3D data and of $J_{\text{interface}}$ and J_{mixed} at short circuit.

Simulation	W_O [nm]	$J_{\text{sc,interface}}$ [A m^{-2}]	$J_{\text{sc,mixed}}$ [A m^{-2}]	$\%_{interface}$	$\%_{mixed}$
1	0	0	24.29	0	100
2	12	8.36	13.78	37.8	62.2
3	0	0	98.17	0	100
7	12	10.50	14.12	42.6	57.4
8	12	10.76	13.78	43.8	56.2
9	12	8.12	14.12	36.5	63.5
10	9	6.23	14.22	30.5	69.5
11	16	11.32	13.17	46.2	53.8
12	9	6.21	14.52	30.0	70.0
13	15	10.55	36.41	22.5	77.5
14	10	5.78	23.86	19.5	80.5
15	8	3.67	21.44	14.6	85.4
16	12	4.02	15.49	20.6	79.4
17	12	16.13	12.62	56.1	43.9
18	8	11.25	12.32	47.7	52.3

4.4 Conclusion

We presented a 3D drift-diffusion model that can consistently simulate the JV characteristics of organic BHJs, including the diffusion and quenching of excitons, the effects of space charge, the recombination and generation of charge carriers and the injection/extraction of carriers at the contacts. With this model we studied the effects that the occurrence of large domains of pure acceptor material has on the efficiency of the devices. We treated each morphological feature, such as the size and shape of the domains, the composition of the mixed phase, the presence of skin layers, independently from the others. Thus, we have been able to disentangle the effect of different aspects of the active layer on the efficiency of the device.

The formation of large acceptor domains is detrimental for the efficiency for two reasons: it reduces the exciton quenching efficiency and it deprives the surrounding mixed phase of acceptor molecules. As a consequence of the low concentration of acceptor in the mixed phase the transport of electron in this phase is not efficient and the photocurrent becomes space-charge limited. We demonstrated how the addition of acceptor to the matrix, keeping the size of the pure domains constant, has a strong beneficial effect on the efficiency. The reduction of the size of the domains, enhancing the exciton quenching efficiency, has also a beneficial impact on the performance of the device, though less evident.

We included in our model the presence of skin layers of donor-rich phase at either electrode. A skin layer at the anode enhances the extracted photocurrent, because it reduces the exciton quenching at the anode and increase the number of photogenerated charges at the donor/acceptor interface. A skin layer at the cathode does not have such an effect: the free holes generated in this layer are not able to be collected at the anode, because the distance that they should travel laterally along the acceptor domain is too large (hundreds of nm) and they are lost via recombination process. Thus, no effect was observed when a skin layer was added at the cathode.

We defined two components for the total current, one coming from the interfacial region between the acceptor phase and the mixed phase, the other coming from the mixed phase. Both the contributions can be simulated with a 1D drift-diffusion numerical code, and them summed to give the total current. This "parallel approach" is based on the lateral movement of electrons in the mixed phase towards the acceptor domains, to be subsequently transported to the cathode. The extent of the lateral movement of electrons depends on the composition of the matrix and on the size of the acceptor domains, and defines which of the two currents dominates. We used the parallel model to fit the data generated by the 3D simulations. In most cases, the current from the mixed phase has been observed to be the dominant component. This explains why the composition of the matrix has the strongest impact on the efficiency of the devices.

The 3D model is a powerful tool that can give a detailed understanding of the physics occurring in the active layer, and a hint on how to optimize the morphology of the active layer. Splitting the current in two components and applying the 1D parallel approach facilitates the interpretation of experimental data, by identifying which region of the active layer dominates the performance of the devices.

References

[1] S. van Bavel, S. Veenstra, J. Loos, *Macromol. Rapid Commun.* **2010**, *31*, 1835.

[2] M. A. Ruderer, P. Müller-Buschbaum, *Soft Matter* **2011**, *7*, 5482.

[3] F. Liu, Y. Gu, J. W. Jung, W. H. Jo, T. P. Russel, *J. Polym. Sci. Part B* **2012**, *50*, 1018.

[4] M. Dante, A. Garcia, T.-Q. Nguyen, *J. Phys. Chem. C* **2009**, *113*, 1596.

[5] J. Guo, H. Ohkita, H. Benten, S. Ito, *J. Am. Chem. Soc.* **2010**, *132*, 6154.

[6] B. A. Collins, Z. Li, J. R. Tumbleston, E. Gann, C. R. McNeill, H. Ade, *Adv. Energy Mater.* **2013**, *3*, 65.

[7] C. R. McNeill, B. Watts, L. Thomsen, W. J. Belcher, N. C. Greenham, P. C. Dastoor, *Nano Lett.* **2006**, *6*, 1202.

[8] B. A. Collins, E. Gann, L. Guignard, X. He, C. R. McNeill, H. Ade, *J. Phys. Chem. Lett.* textbf2010, *1*, 3160.

[9] W. C. Tsoi, S. J. Spencer, L. Yang, A. M. Ballantyne, P. G. Nicholson, A. Turnbull, A. G. Shard, C. E. Murphy, D. D. C. Bradley , J. Nelson, J. S. Kim, *Macromol.* **2011**, *44*, 2944.

[10] M. J. Im, S. Y. Son, B. J. Moon, G. Y. Lee, J. H. Kim, *Organic Electron.* **2013**, *14*, 3046.

[11] J. A. Bartelt , Z. M. Beiley, E. T. Hoke, W. R. Mateker, J. D. Douglas, B. A. Collins, J. R. Tumbleston, K. R. Graham, A. Amassian, H. Ade, J. M. J. Fréchet, M. F. Toney, M. D. McGehee, *Adv. Energy Mater.* **2013**, *3*, 364.

[12] L. J. A. Koster, *Phys. Rev. B* **2010**, *81*, 205318.

[13] S. E. Shaheen, C. J. Brabec, N. S. Sariciftci, F. Padinger, T. Fromherz, J. C. Hummelen, *Appl. Phys. Lett.* **2001**, *78*, 841.

[14] T. Martens, J. D'Haen, T. Munters, Z. Beelen, L. Goris, J. Manca, M. D'Olieslaeger, D. Vanderzande, L. De Schepper, R. Andriessen, *Synt. Metals* **2003**, *138*, 243.

[15] H. Hoppe, M. Niggemann, C. Winder, J: Kraut, R. Hiesgen, A. Hinsch, D. Meissner, N. S. Sariciftci, *Adv. Funct. Mater.* **2004**, *14*, 1005.

[16] M. M. Wienk, M. Turbiez, J. Gilot, R. A. J. Janssen, *Adv. Mater.* **2008**, *20*, 2556.

[17] F. Zhang, K. G. Jespersen, C. Björström, M. Svensson, M. R. Andersson, V. Sundström, K. Magnusson, E. Moons, A. Yartsev, O. Inganäs, *Adv. Funct. Mater.* **2006**, *16*, 667.

[18] Q. D. Dao, T. Hori, K. Fukumura, T. Masuda, T. Kamikado, A. Fujii, Y. Shimizu, M. Ozaki, *Organic Electronics* **2013**, *14*, 2628.

[19] G. Li, V. Shrotriya, J. Huang, Y. Yao, T. Moriarty, K. Emery, Y. Yang, *Nat. Mater.* **2005**, *4*, 864.

[20] B. Schmidt-Hansberg, M. Sanyal, M. F. G. Klein, M. Pfaff, N. Schnabel, S. Jaiser, A. Vorobiev, E. Müller, A. Colsmann, P. Scharfer, D. Gerthsen, U. Lemmer, E. Barrena, W. Schabel, *ACS Nano* **2011**, *5*, 8579.

[21] M. Pfaff, M. F. G. Klein, E. Müller, P. Müller, A. Colsmann, U. Lemmer, D. Gerthsen, *Micros. Microanal.* **2012**, *18*, 1380.

[22] H.-Y. Chen, J.-L. Wu, C.-T. Chen, C.-T. Chen, *Chem. Commun.* **2012**, *48*, 1012.

[23] K. Maturová, M. Kemerink, M. M. Wienk, D. S. H. Charrier, R. A. J. Janssen, *Adv. Funct. Mater.* **2009**, *10*, 1379.

[24] K. Maturová, S. S. van Bavel, R. A. J. Janssen, M. Kemerink, *Nano Lett.* **2009**, *9*, 3032.

[25] L. J. A. Koster, O. Stenzel, S. Oosterhout, M. M. Wienk, V. Schmidt, R. A. J. Janssen, *Adv. Energy Mater* **2013**, *3*, 615.

[26] P. K. Watkins, A. B. Walker, G. L. B. Verschoor, *Nano Lett.* **2005**,*5*, 1814.

[27] C. Groves, R. G. E. Kimber, A. B. Walker, *J. Chem. Phys.* **2010**, *133*, 144110.

[28] J. C. Bijleveld, V. S. Gevaerts, D. Di Nuzzo, M. Turbiez, S. G. J. Mathijssen, D. M. de Leeuw, M. M. Wienk, R. A. J. Janssen, *Adv. Mater.* **2010**, *22*, E242.

[29] C. M. Amb, S. Chen, K. R. Graham, J. Subbiah, C. E. Small, F. So, J. R. Reynolds, *J. Am. Chem. Soc.* **2011**, *133*, 10062.

[30] E. G. Wang, Z. Ma, Z. Zhang, K. Vandewal, P. Henriksson, O. Inganäs, F. Zhang, M. R. Andersson, *J. Am. Chem. Soc.* **2011**, *133*, 14244.

[31] R. Stalder, C. Grand, J. Subbiah, F. So, J. R. Reynolds, *Polym. Chem.* **2012**, *3*, 89.

[32] L. J. A. Koster, E. C. P. Smits, V. D. Mihailetchi, P. W. M. Blom, *Phys. Rev. B* **2005**, *72*, 085205.

[33] A. A. Bakulin, J. C. Hummelen, M. S. Pshenichnikov, P. H. M. van Loosdrecht, *Adv. Funct. Mater.* **2010**, *20*, 1653.

[34] P. Langevin, *Ann. Chim. Phys* **1903**, *28*, 433.

[35] G. Juška, K. Arlauskas, J. Stuchlik, R. Österbacka, *J. Non-Cryst. Solids* **2006**, *352*, 1167.

[36] G. Juška, K. Genevičius, N. Nekrašas, G. Sliaužys, R. Österbacka, *Appl. Phys. Lett.* **2009**, *95*, 013303.

[37] S. Selberherr, *Analysis and simulation of semiconductor devices*. Springer Science & Business Media, Wien, 2012.

[38] V. D. Mihailetchi, J. Wildeman, P. W. M. Blom, *Phys. Rev. Lett.* **2005**, *94*, 126602.

[39] S. Kouijzer, J. J. Michels, M. van den Berg, V. S. Gevaerts, M. Turbiez, M. M. Wienk, R. A. J. Janssen,. *J. Am. Chem. Soc.* **2013**, *135*, 12057.

[40] B. P. Lyons, N. Clarke, C. Groves, *J. Phys. Chem. C* **2011**, *115*, 22572.

[41] L .J. A. Koster, V. D. Mihailetchi, R. Ramaker, P. W. M. Blom, *Appl. Phys. Lett.* **2005**, *86*, 123509.